Available online at www.sciencedirect.com
ScienceDirect
ELSEVIER
International Journal of Solids and Structures 44 (2007) 5680–5694
INTERNATIONAL JOURNAL OF SOLIDS AND STRUCTURES
www.elsevier.com/locate/ijsolstr

Integrated numerical–experimental analysis of interfacial fatigue fracture in SnAgCu solder joints

M. Erinc, P.J.G. Schreurs *, M.G.D. Geers

Eindhoven University of Technology, Department of Mechanical Engineering, Section of Materials Technology, 5600MB, Eindhoven, The Netherlands

Received 21 March 2006; received in revised form 10 January 2007
Available online 25 January 2007

Abstract

In ball grid array (BGA) packages, solder balls are exposed to cyclic thermo-mechanical strains arising from the thermal mismatch between package components. Thermo-mechanical fatigue crack propagation in solder balls is almost always observed at the chip side of the bump/pad junction. The objective of the experimental part of this study is to characterize the bump/pad interface under fatigue loading. Fatigue specimens are prepared by reflowing Sn3.8Ag0.5Cu lead-free solder alloy on Ni/Au substrates. Obtained results show that fatigue damage evolution strongly depends on the microstructure. Applied strain and solder volume both have an influence on the fatigue damage mechanism. In the numerical part of the study, fatigue experiments are modeled using the finite element technique. A cohesive zone approach is used to predict the fatigue damage evolution in soldered connections. Crack propagation is simulated by an irreversible linear traction–separation cohesive zone law accompanied by a non-linear damage parameter. Cohesive zone elements are placed where failure is experimentally observed. Damage evolution parameters for normal and tangential interaction are scrutinized through dedicated fatigue tests in pure tensile and shear directions. The proposed cohesive zone model is quantitatively capable of describing fatigue failure in soldered joints, which can be further extended to a numerical life-time prediction tool in microelectronic packages.
© 2007 Elsevier Ltd. All rights reserved.

Keywords: Lead-free solder; Cohesive zone modeling; Low-cycle fatigue

1. Introduction

Miniaturization trend in microelectronics has recently led to the development of ball grid array (BGA) and flip-chip packages. As size gets smaller, local operating temperatures increase, hence the package components are exposed to higher mechanical strains. In service use, thermal expansion coefficient mismatch between the package components leads to cyclic thermo-mechanical strains. In a microelectronic package, solder balls are prone to thermo-mechanical fatigue failure (Fig. 1), which results in an open circuit and causes the electronic

* Corresponding author. Tel.: +31 40 2472778; fax: +31 40 2447355.
E-mail address: p.j.g.schreurs@tue.nl (P.J.G. Schreurs).

0020-7683/$ - see front matter © 2007 Elsevier Ltd. All rights reserved.
doi:10.1016/j.ijsolstr.2007.01.021

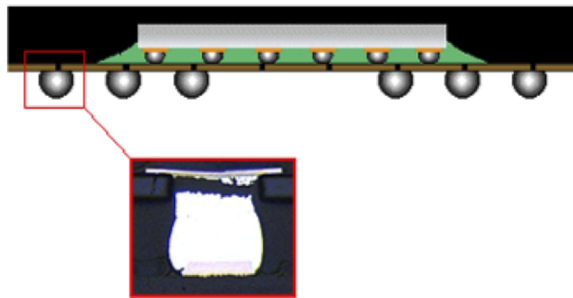

Fig. 1. Cross-section of a ball grid array and a failed corner solder bump, courtesy of Dr. JWC. de Vries, Philips Applied Technologies.

device to stop functioning. Another consequence of miniaturization is that in small parts mechanical properties become inhomogeneous due to size effects. It is previously reported by Matin (2005) that these size effects cause microstructure driven damage localization in lead-free solders. Therefore, an in-depth study relating microstructure and fatigue damage evolution is crucial for the physical understanding of the thermo-mechanical fatigue problem in solder joints.

From July 2006 on, lead (Pb) containing parts are not used in microelectronic packages due to legislation. Among lead-free alternatives SnAgCu is a widely accepted lead-free replacement due to its better creep-fatigue resistance and microstructural stability. A broad review on lead-free solders in microelectronics is given by Abtew and Seldavuray (2000). Microstructural evolution in annealed cast SnAgCu alloy is studied by Allen et al. (2004). In their study, eutectic intermetallic components were found to coarsen, however the rate of reaction was significantly slower than in SnPb solder. On bond pads, Ni/Au is the most widely used surface finish. Interfacial structure between SnAgCu and Ni/Au metallization has been extensively studied (Zeng et al., 2002; Ratchev et al., 2004; Sharif and Chan, 2005; Yoon et al., 2005; Erinc et al., 2005). Solders are exposed to high homologous temperatures in service, therefore, in microstructural and mechanical characterization, evaluation of time-dependent properties becomes crucial. Time-dependent material behavior of SnAgCu in connection with microstructure is studied in detail (Wiese et al. (2002); Wiese and Wolter (2004); Lin and Chu (2005)). A review on solder joint fatigue models is given by Lee et al. (2000). However, experimental validation of these models at the level of a single solder interconnect is hardly existing in the literature. A chip size experimental and numerical study of SnPb solder fatigue fracture is carried out by Towashiraporn et al. (2005).

Fatigue life predictions for solder joints are generally carried out by using a Coffin-Manson rule or a similar empirical relationship, where the solder material is treated as a homogenous continuum. Driven by miniaturization, solder joints have become so small that the size of microstructural entities in the solder is comparable to that of the joint itself. In order to predict fatigue failure at these size scales, rather than scale independent continuum-based approaches, local damage formulations in the solder joint are needed.

The objective of this study is: (1) to establish a link between microstructure and damage in lead-free solder joints under cyclic mechanical loading, (2) to characterize fatigue damage evolution at the bond/pad interface and (3) to simulate local deformations leading to fatigue crack propagation by separation of interfaces. As motivated above, eutectic SnAgCu is here selected as the lead-free solder alloy of interest, and Ni/Au as the substrate in order to incorporate the full metallurgy at the bump/pad interface. In commercial packages, Ni is used as a diffusion barrier between Cu and solder, therefore no Cu is needed in the test specimens. It has been previously shown by the authors that the crack path between Ni/Au substrate and SnAgCu follows physical boundaries in the microstructure (interfaces) and the crack propagation can be split into normal and tangential components (Erinc et al., 2005). Such an interfacial failure scheme can be modeled effectively with a cohesive zone approach. In the cohesive zone formulation used in this study, normal and tangential tractions are decoupled. Therefore, two sets of experiments are set up; specimens that will induce pure tensile loading at the solder/metallization interface, and specimens that will induce pure shear loading at the solder/metallization interface. Later, tensile experiments are used to characterize the cohesive zone parameters for normal opening, and shear experiments are used to characterize the cohesive zone parameters for tangential opening.

Ni/Au–SnAgCu fatigue specimens are cyclically loaded with constant amplitude. Fatigue life is determined by the decrease in the reaction force. Experimental procedures and the results of fatigue tests are explained in

Sections 2.1 and 2.2, respectively. For every fatigue test sample, the stress–strain data as a function of number of cycles is plotted. Individual fatigue test samples are modeled using the finite element technique. Cohesive zone elements are placed at the regions where failure is observed. In Section 3, the cohesive zone model used in this study, and the details of inverse parameter estimation is discussed. Lastly, a solder ball is modeled in 2D, and the fatigue life is predicted using the cohesive zone model explained in Section 4.

2. Fatigue tests

2.1. Experimental procedure

First, mechanical properties of the materials that are going to be used in fatigue tests are measured. For this purpose, two half tensile parts are soldered with Sn3.8Ag0.5Cu. In order to be able to measure the Young's modulus for soft materials like solders, very small strains should be measured with high accuracy. Contact strain measuring techniques at these small scales may induce undesired effects, i.e., sliding of extensometer legs, holes for extensometer pins. For this reason, a non-contact optical strain mapping method is used. The specimen is first sprayed to create a fine distribution of black dots on white background. The tensile test is carried out in situ under an optical microscope and high resolution digital images are acquired periodically by a digital camera. These images are then uploaded to (Aramis v5.3.0, 2004) strain mapping software where local strains are calculated by masking the substrate. The soldered joint was 200 μm thick and 10 mm long. Since image acquisition time is known in advance, the images captured are synchronized with the force–time recording and thereby a stress–strain curve is obtained. For SnAgCu, Young's modulus and yield stress is measured as 51 GPa and 25.24 MPa, respectively. Initial yield stress is taken as the engineering stress at 0.2‰ strain offset. The stress–strain curve for Sn3.8Ag0.5Cu is shown in Fig. 2; the associated hardening rule is determined from the experimental data points.

Two sets of fatigue experiments, being pure tensile and pure shear are set up. The specimen geometries are shown in Fig. 3. First, Ni substrates are machined from 1 mm thick 99.98% purity nickel plates by wire-erosion using an electro-discharge machine (EDM). Except for the external faces to be soldered, machined parts are teflon-coated in order to prevent excessive wetting of the solder on nickel. Next, the surface to be soldered is Au coated by ion sputtering to a thickness of 0.5–0.8 μm, which represents a typical printed circuit board (PCB) bump/pad. Ni/Au substrates are soldered by Sn3.8Ag0.5Cu solder flux on a hot plate at 250 °C and air cooled. Metallographic surface preparation is applied on both sides of the sample. All specimens were 5 cm in the longest axis and <1 mm in thickness (due to grinding). For the tensile specimens, four different geometries are considered; the gage width, shown with an arrow in Fig. 3a, is taken as 10, 5, 3 and 1 mm. Two 10 mm, six 5 mm, eight 3 mm and eight 1 mm specimens are produced. For the double joint shear specimens, two different geometries are considered: the gage width is taken as 3 and 1 mm (Fig. 3b). Three specimens for each double

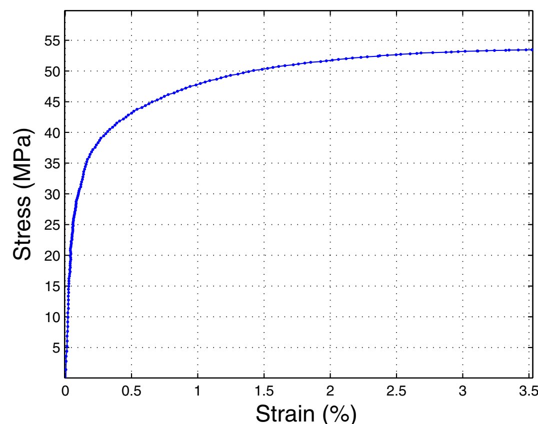

Fig. 2. Stress–strain curve for Sn3.8Ag0.5Cu.

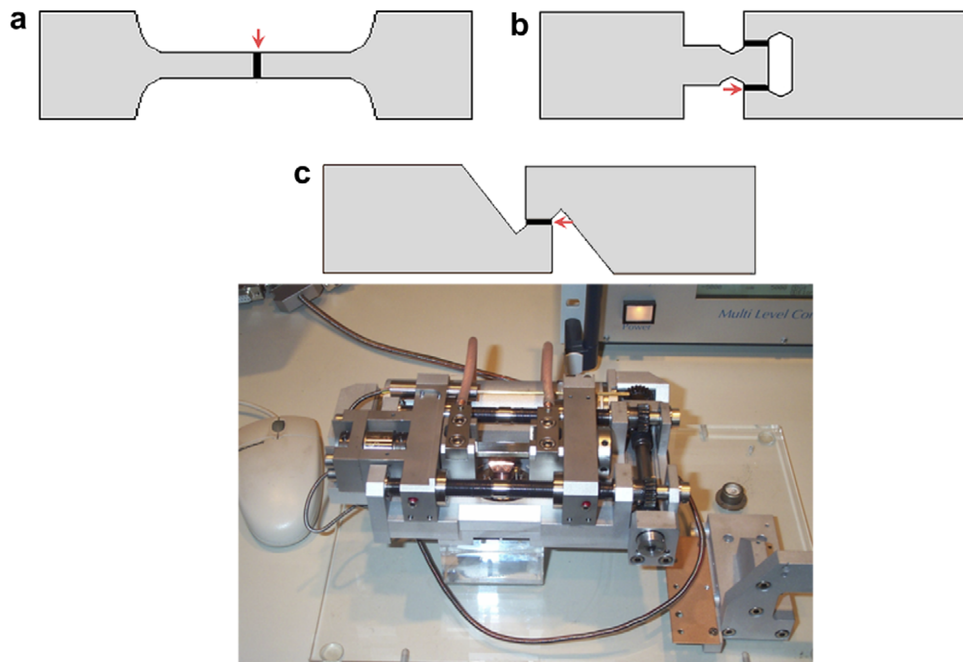

Fig. 3. Sn3.8Ag0.5Cu–Ni/Au soldered joints of shape: (a) tensile, (b) double joint shear, (c) single joint shear (left). Double spindle micro-tensile stage (right).

joint geometry is produced. For the single joint shear specimens, nine 3 mm gage specimens are produced (Fig. 3c). Polished samples are first examined under polarized light, where grains and solder dimensions are measured. The solder thickness varied between 500 ± 200 μm. On average, the solder volume in 10, 5, 3 and 1 mm tensile samples was ∼4, ∼2, ∼2 and ∼0.4 mm^3, respectively. The 3 mm double joint shear specimens contained ∼1.2 mm^3, and 1 mm contained ∼0.4 mm^3 solder. Single joint shear specimens contained ∼1.2 mm^3 solder.

Fatigue tests were conducted in a computer controlled double spindle micro-tensile stage (Kammrath & Weiss) where reaction force and elongation were recorded. An external extensometer and a 500 N load cell was used. Clamp speed was set to 1–2 μm/s depending on experimental convenience. Triangular cyclic elongation was prescribed. Tests took place at constant room temperature. The solder joint was considered as failed when the recorded reaction force dropped to half of the maximum stress attained in the first cycle, and the corresponding number of cycles is referred as the solder joint's strain life (half life criterion: Metals Handbook (1985)). Strain applied to solder joints varied in the range −1% to 3.5%.

2.2. Results

Fig. 4 shows the local strain field distribution in a soldered joint under tensile loading at various global strain values. SnAgCu solder is situated in the middle and on the left and right is the Ni/Au substrate. Strain fields are monitored throughout the deforming region until 1% strain level is reached. Strain is distributed homogeneously at the start of experiment, up to a threshold value of ∼0.04%. After 0.04% global strain, local strain fields at the bonding interfaces are observed to be higher than the strain in the bulk solder, indicating damage localization. With further increase in global strain, a fairly homogeneous strain distribution in the solder in between the interfacial regions is seen. At 0.5% global strain, local strain in the solder corresponds to ∼4%, which is well in the plastic region. At later stages, crack propagation is observed on the interfacial regions having the highest local strain values. Post-mortem analysis shows that regions near the solder interface are heavily deformed. Fig. 5 shows an $(Cu,Ni)_6Sn_5$ intermetallic that has delaminated from the solder

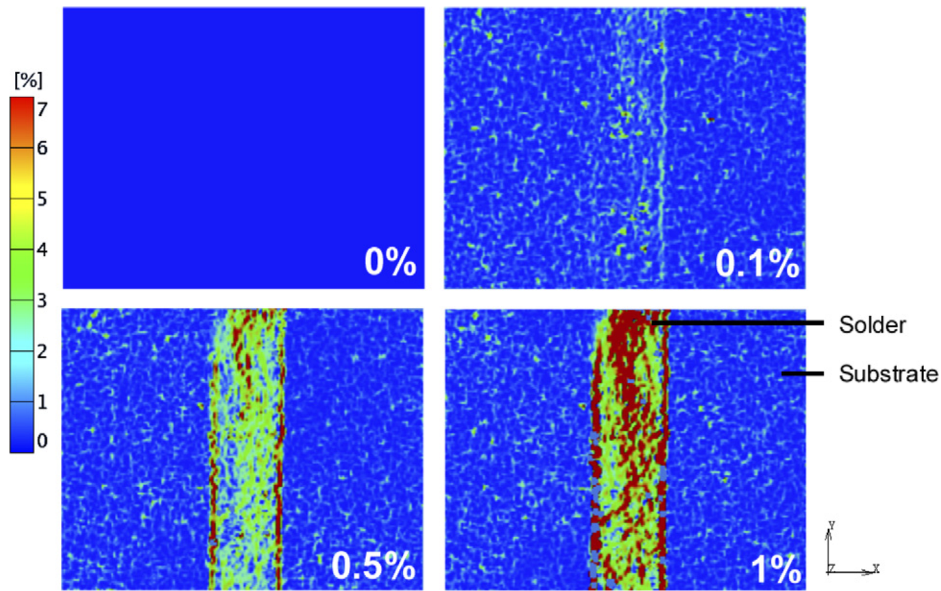

Fig. 4. Local strain field distribution in Ni/Au–SnAgCu–Ni/Au solder joint having global strain values $\varepsilon_{xx} = 0\%$, 0.1%, 0.5% and 1%.

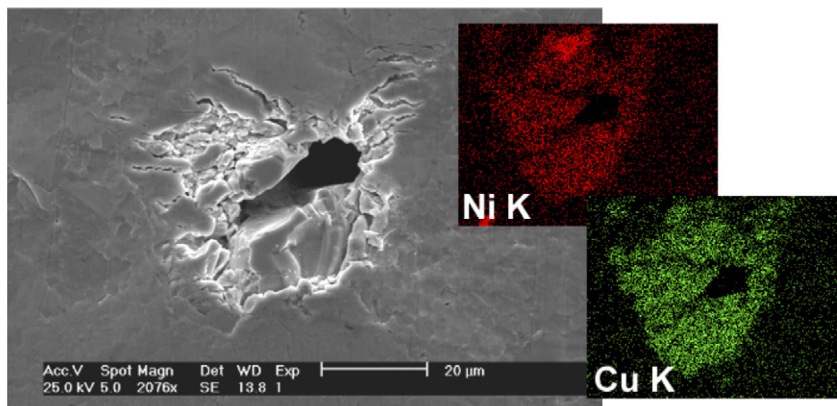

Fig. 5. Upon tensile loading, $(Cu,Ni)_6Sn_5$ intermetallic compound has cracked into pieces and initiated secondary cracks in the surrounding solder matrix.

matrix and cracked, thereby triggered secondary crack initiation in the solder surrounding the intermetallic. Intermetallic compounds form during reflow and they act as stress concentration points due to their sharp edges. Furthermore, they are more brittle than the matrix ($\text{Hardness}_{Cu_6Sn_5} = 3.7$ GPa, $\text{Hardness}_{SnAgCu} = 0.83$ GPa Erinc et al. (2004)).

2.2.1. Failure types

As mentioned previously, in this study fatigue failure is defined as the number of cycles when the reaction force has dropped to half of the initial value. If the sample did not fail before 10,000 cycles, the test was stopped due to time limitations. For every fatigue specimen, stress versus number of cycles is plotted. Results can be categorized in one of the three following schemes: a delamination regime (type A), an infinite life regime (type C), and in between type A and C, a gradual failure regime (type B). Microstructural observations suggest that there are two different failure mechanisms operative: (1) heterogeneous matrix deformation and (2)

localization of deformation at the bonding interface. Failure types A, B and C and the corresponding micrographs are shown in Fig. 6.

Type A failure can be examined in three stages: (1) incubation period in the beginning where stress reached at peak strain is steady, (2) fatigue failure stage where stress at peak strain decreases steeply and (3) the last stage where stress decreases gradually which is believed to be due to crack bridging and friction. Fractographs show highly localized damage at the bonding interface since the major crack propagates on the interface and there is almost no matrix deformation. If there are blowholes in the solder, main crack preferentially propagates on that weaker interface. Here the dominating failure mechanism is delamination. Strain life is between 1000 and 2000 cycles. Type A failure is observed in the fatigue specimens in which the initial stress was highest. In addition, solder volume being less than ~1 mm^3 seemed to increase the tendency towards delamination.

An infinite fatigue life (type C) is observed when the initial stress was less than 17 MPa, and/or when solder volume exceeded 3 mm^3. This suggests that strain life of SnAgCu solder joints is not only determined by the initial stress state but also depends on geometry. In the solder matrix many small cracks are observed. The pattern of these cracks coincides with the pattern observed in the polarized images taken before the fatigue

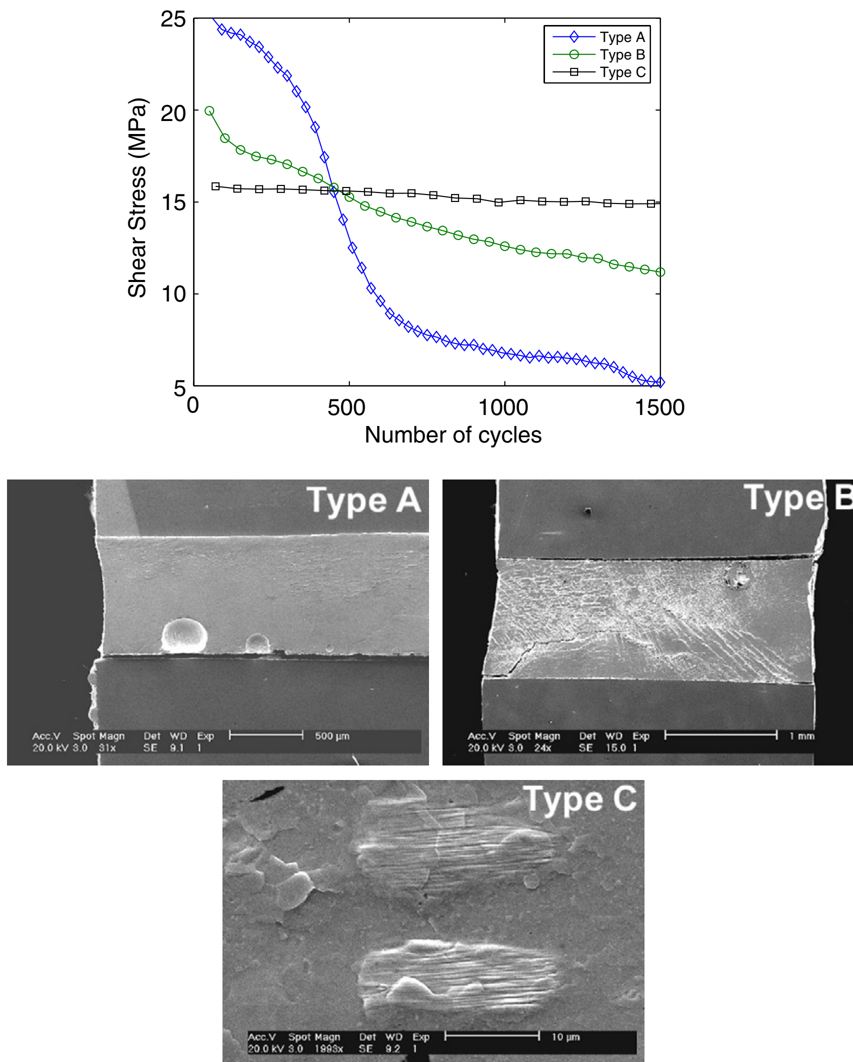

Fig. 6. Stress drop regimes observed in cyclic strain controlled experiments and typical micrographs corresponding to A, B and C failure types.

tests. This suggests for the present case that fatigue cracks initiate on domain boundaries where there is a slight difference in the crystallographic orientation. Another interesting observation is that slip lines appeared in β-Sn dendrite arms. Slip lines are not observed in the eutectic matrix because the intermetallic components of the ternary eutectic matrix (i.e., eutectic Ag_3Sn and eutectic Cu_6Sn_5) are pinning points for dislocation movement, whereas β-Sn is almost only Sn. In type C specimens, a major fatigue crack was still not observed after 10,000 cycles. Our experiments suggest that there is a fatigue limit in both normal and tangential directions of the bonding interface, with a roughly estimated value of $\sigma_f = 17$ MPa. However, a separate testing procedure is necessary to determine the fatigue limit of the interface and its dependence on solder geometry more accurately.

Specimens in which fatigue failure proceeds gradually are referred as type B. Fractographs show heavy matrix deformation as well as an interfacial fatigue crack which has led to failure. Surface relief in the solder matrix consists of slip in β-Sn dendrites, many short cracks on domain boundaries in the eutectic matrix, parallel deformation bands 45° to the loading direction, and secondary fatigue crack propagation on grain boundaries. Strain life is between 2000 and 5000 cycles. Here, both deformation mechanisms mentioned above are operative.

Whether the fracture behavior will be abrupt (by delamination) or gradual depends on local soldering conditions. Existence of manufacturing defects on the surface, less wetting, less intermetallic growth will favor delamination leading to a sudden failure. If the fatigue crack propagation is taking place in the solder very close to the bump/pad, dimples and fatigue striations are observed in the fractographs and the expected failure type is gradual.

Shear specimens show more matrix deformation than tensile specimens. This suggests that the interfacial region is weaker in the normal direction than in the tangential direction. In the tangential direction, the scallop geometry of intermetallic compounds serve as a mechanical barrier and solder cannot delaminate easily. Therefore, energy dissipation due to plastic deformation in the matrix is promoted over damage localization at the bonding interface.

2.2.2. *Size effect*

Results of the fatigue tests are classified according to specimen geometry. Strain life versus applied strain for four different types of tensile specimens, i.e., gage width being 10, 5, 3 and 1 mm, are shown in Fig. 7a. Indicated strain values are corrected for the elongation in the substrate and thus correspond to the actual strain in the solder. For the shear specimens, strain life versus initial shear stress is plotted in Fig. 7b for three different types of shear specimens indicated in the figure. Comparison is made on the basis of both applied strain and initial stress. Applied strain is directly related to the fatigue life, however, during specimen preparation (grinding and polishing), sample thickness decreases differently for different samples and comparison

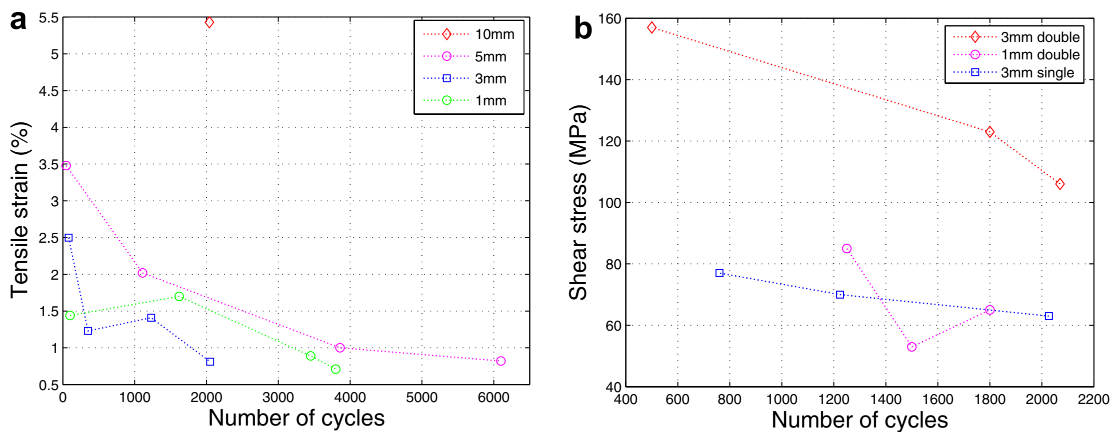

Fig. 7. Strain life versus (a) strain on solder and (b) initial stress, for tensile and shear specimens.

with respect to stress takes into account the difference in cross-section. It is clearly seen that there is a size driven trend in the fatigue lives of both tensile and shear specimens. As the gage width decreases, fatigue life under the same initial stress also decreases. Apparently, a smaller solder volume increases the tendency towards localized deformations at the bonding interfaces. Interestingly, 1 mm gage tensile specimens do not follow this pattern; strain life of 1 mm specimens is higher than 3 mm specimens. This can be explained in the following way: the probability of having casting defects in a smaller volume is less than the probability of having a defect in a bigger volume. Since fatigue cracks initiate at the surface or at defects, 1 mm tensile specimens have a smaller surface area and apparently contain less defects. To summarize, for SnAgCu–Ni/Au soldered joints, smaller joints are weaker than bigger joints until 0.4 mm^3 solder volume. Our results agree with previous studies given by Visser (2002) and confirm that mechanical properties of soldered joints are size dependent.

2.2.3. Fractography

It was possible to examine the fracture surfaces in cases where fatigue samples fell apart in two pieces. Some examples of fatigue fracture surfaces between SnAgCu and Ni/Au are shown in Fig. 8. In Fig. 8a, b and c, ductile fracture patterns are seen. Dimple formation and striations are clearly visible. On the substrate side of the fracture surface, scallop heads of the interfacial intermetallic compound Ni_3Sn_4 are seen. This suggests that delamination starts from scallop tips and the fatigue crack propagates by coalescence of these voids. In some instances, solder has completely delaminated from the substrate. In delaminated samples, only the intermetallic compounds that form during reflow were visible on the substrate side (Fig. 8d).

In Fig. 9a, reaction force is plotted against number of cycles (N) for a 3 mm tensile specimen. As fatigue deformation initiates, the upper part of the F–N plot approaches x-axis as a result of damage evolution and crack growth. However, the lower part of the curve also approaches x-axis where it is expected to remain constant. Fig. 9b shows the lateral cross-section of the specimen where the solder moved out of the sample plane. Apparently, due to crack propagation material continuity is lost at a point and grains are free to move out-of-plane. Since the in-plane material volume decreases by this movement, the external force required to displace the material back to its original in-plane position also decreases.

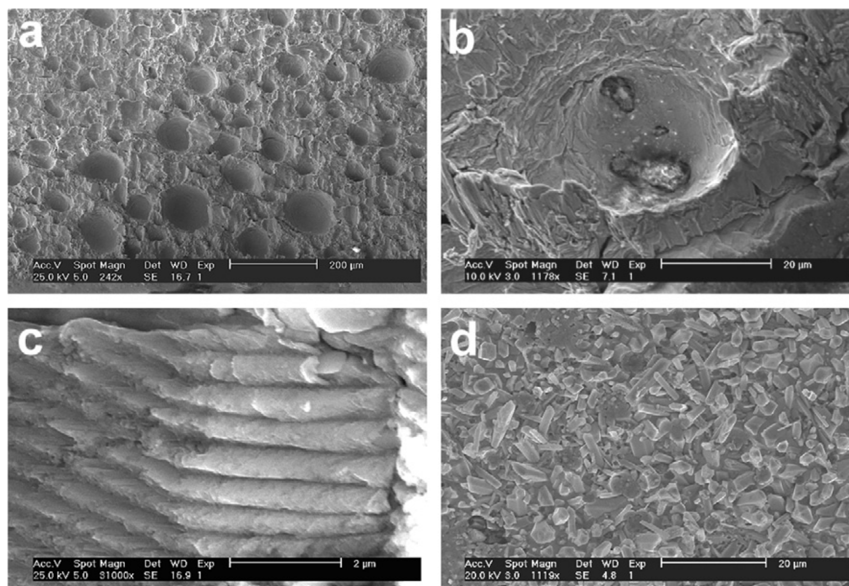

Fig. 8. Fatigue fracture surfaces at the bonding interface: (a) dimples on solder side, (b) corresponding dimples on substrate side, (c) fatigue striations, (d) delamination surface on substrate side.

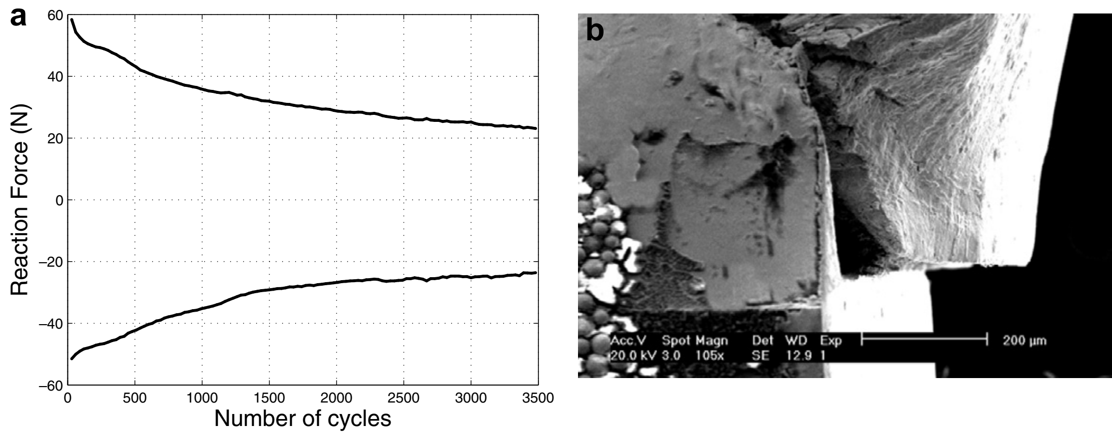

Fig. 9. (a) *F–N* plot of a 3 mm tensile specimen, (b) lateral view of the specimen after 3500 cycles.

3. Cohesive zone model (CZM)

Cohesive zones were developed to model crack initiation and propagation as the separation between two surfaces resisted by cohesive tractions (Dugdale, 1960; Barenblatt, 1962; Needleman, 1990). Static cohesive zone models are extended to model interfacial failure under cyclic loading (Foulk et al., 1998), whereas other models have been proposed on the basis of the incorporation of a damage parameter (de-Andres et al., 1999). Based on previous formulations (Roe and Siegmund, 2003) an irreversible damage model for interface fatigue crack growth is described. A damage variable D is introduced in the model which evolves from the undamaged state $D = 0$, until complete failure $D = 1$. As damage increase, the apparent stiffness $k(1 - D)$ in Eq. (1), where k is the initial stiffness, diminishes until no traction is needed for separation. In Fig. 10a, a schematic representation of a cohesive zone model is shown, where two surfaces are attached by two perpendicular springs, which allows the two surfaces to be separated from each other in the tangential (t) and the normal (n) directions. Fig. 10b shows the cohesive traction T as a function of opening displacement Δ for various number of cycles. A cyclic sinusoidal displacement is applied to the upper nodes and the lower nodes are restricted. As maximum opening displacement increases, maximum traction decreases as a result of damage evolution via cyclic loading. Abdul-Baqi et al. (2005) modeled the thermo-mechanical fatigue damage in solder balls by this cohesive zone approach and proposed a damage evolution law specific to solder materials. Damage evolution is determined by Eq. (2) where $\dot{\Delta}_\alpha$ is the rate of relative opening, σ_f is the fatigue limit, c, m and r are constants that control the rate of D and thus the decay of the cohesive interaction. The cohesive zone formulation is implemented in the commercial finite element package MSC.Marc/Mentat as a user defined element in 2D (Van den Bosch et al., 2006) which can be used both in-plane strain and in-plane stress to describe the interfacial interaction.

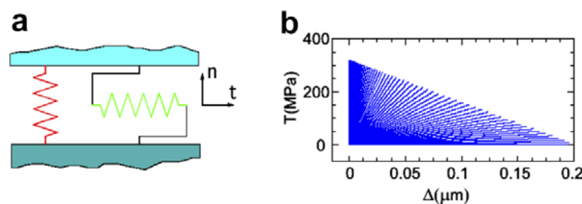

Fig. 10. (a) Spring model for a cohesive zone element, (b) cohesive traction versus opening for various number of cycles.

$$T_{\rm n} = k_{\rm n}(1 - D_{\rm n})\Delta_{\rm n}, \quad T_{\rm t} = k_{\rm t}(1 - D_{\rm t})\Delta_{\rm t} \tag{1}$$

$$\dot{D}_{\rm n,t} = c_{\rm n,t}|\dot{\Delta}_{\rm n,t}|(1 - D_{\rm n,t} + r_{\rm n,t})^{m}_{\rm n,t}\left\langle \frac{|T_{\rm n,t}|}{1 - D_{\rm n,t}} - \sigma_{\rm f} \right\rangle \tag{2}$$

3.1. Characterization of CZM

As confirmed by the present fatigue experiments, thermo-mechanical fatigue cracks in solder joints almost always follow the bonding interface. In order to simulate this failure mechanism, cohesive zone elements are placed at the intermetallic/solder interface. Since all physical interfaces have a very small, though a finite thickness, the interfacial zone is given 100 nm initial thickness ($t_{\rm cz}$). In classical cohesive zone approaches, cohesive zones do not need to have an initial thickness. However, assigning a finite thickness allows one to calculate a finite initial stiffness which prevents the known initial stiffness problem and also describes the interphase (Chaboche et al., 2001). Initial stiffness of the cohesive elements for normal ($k_{\rm n}$) and tangential ($k_{\rm t}$) directions are computed from the adjacent materials 1 and 2, in order to provide an equivalent elastic deformation initially with and without the cohesive elements. Initial stiffness for tangential and normal directions are given by:

$$k_{\rm t} = \frac{2G_1G_2}{t_{\rm cz}(G_1 + G_2)}, \quad k_{\rm n} = \frac{2E_1E_2}{t_{\rm cz}(E_1 + E_2)} \tag{3}$$

where E is the Young's modulus and G is the shear modulus. Eq. (3) gives a harmonic mean type of relationship between the initial stiffness of the interface element with its neighbors, depending on the initial thickness of the cohesive element. When $t_{\rm cz}$ goes to zero, $k_{\rm n}$ and $k_{\rm t}$ go to infinity.

As the numerical calculations were initiated, it appeared that two issues were not well addressed in the cohesive zone formulation. During the simulations of tensile specimens, cohesive zone elements start failing after a certain number of cycles which results in a mutual penetration of continuum elements. Second, as emphasized in Section 2.2, in the later stages of tensile fatigue tests, material continuity is lost and some solder grains are free to move out of the sample plane. To account for both issues, an additional correction term $f{*}k_{\rm n}{*}|\Delta_{\rm n}|^e$ is introduced in Eq. (4) to penalize material penetration:

$$T_{\rm n} = \begin{cases} k_{\rm n}(1 - D_{\rm n})\Delta_{\rm n} - f * k_{\rm n} * |\Delta_{\rm n}|^e & \text{if } \Delta_{\rm n} < 0 \\ k_{\rm n}(1 - D_{\rm n})\Delta_{\rm n} & \text{if } \Delta_{\rm n} \geqslant 0 \end{cases} \tag{4}$$

Compression penalty is controlled by the constant f. In-plane material loss due to 3D movement is taken into account by the constant e. In the early stages of loading, the compression penalty dominates over the out-of-plane movement, and the cohesive zone is prohibited from penetrating into neighboring elements. As damage evolves, cohesive zones open up more, $\Delta_{\rm n}$ increases and the out-of-plane movement starts to be significant. A number of calculations have been performed to see the effect of constants in the correction term, which are plotted in Fig. 11. From both a numerical convenience point of view and to represent experimental results best, constants in the correction term are set as $f = 1000$ and $e = 3.7$.

3.2. Parameter determination

Test specimens shown in Fig. 3 are modeled using 2D plane stress elements. Fatigue experiments are simulated by prescribing the real experimental conditions at the specimen boundaries. Cohesive zone elements are placed between the intermetallic compound and solder, where fatigue failure is typically observed. In the simulations, damage evolution parameters are tuned to obtain the same global stress–strain response as measured in the experiments. By modeling the complete test-specimen, experimental stress–strain data is converted indirectly to the traction-displacement in the cohesive zones. A set of damage evolution parameters c, m and r in Eq. (2) is obtained which characterizes the strength of SnAgCu–Ni/Au bonding interface under cyclic strain. Among these, c is related to the damage initiation before any softening starts. The power parameter m takes values between 3 and 3.3, and is responsible from the sharpness of the softening. Parameter r takes values close to 0^+, and is the slope of the softening tail in the last stages of deformation. Smaller values of r predict a longer life time. In the present model, damage evolution is activated during loading alone, and inhibited during

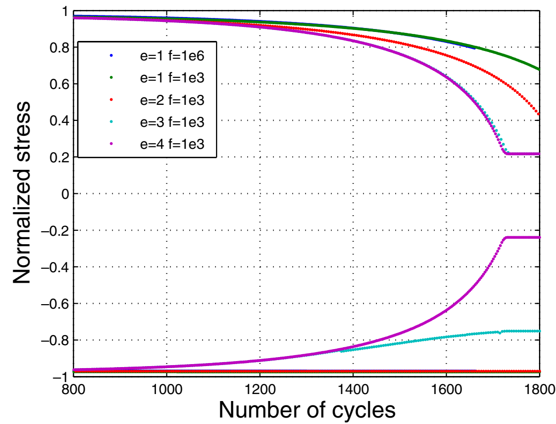

Fig. 11. Effect of constants in the cohesive zone compression correction term.

unloading in the cyclic load sequence. SnAgCu is modeled as indicated in Section 2.1, with Poisson's ratio $\nu = 0.35$. Young's modulus and Poisson's ratio of Ni is taken as 198 GPa and 0.31. Young's modulus of the intermetallic compound Ni_3Sn_4 is reported as 140.4 GPa (Jang et al., 2004), and Poisson's ratio is taken as $\nu = 0.2$. Substrate nickel and the intermetallic compound Ni_3Sn_4 are modeled linear elastically, since the stress state at the peak of the cycle is safely below the yield stress of both materials. Fatigue experiments were conducted at room temperature. SnAgCu is modeled by a time independent elasto-plastic material model combined with a steady-state creep model for bulk SnAgCu given by Wiese and Wolter (2004), shown in Eq. (5) where A_1 and A_2 are 4e-7 and 1e-12 s^{-1}, Q_1 and Q_2 are 26.8 and 61.4 kJ/mol, n_1 and n_2 are 3 and 10 (different from the original value), respectively.

$$\dot{\varepsilon} = A_1\left(\frac{\sigma}{\sigma_N}\right)^{n_1}\exp\left(-\frac{Q_1}{RT}\right) + A_2\left(\frac{\sigma}{\sigma_N}\right)^{n_2}\exp\left(-\frac{Q_2}{RT}\right) \tag{5}$$

Blowholes are a common problem in soldering. A blowhole is a void at the bump/pad junction which decreases the cross-sectional area and therefore decreases the strength of the interface. For this reason, test specimens were examined in the presence of blowholes. In the numerical simulation of these specimens, initial damage in the corresponding cohesive zone elements is set to 1. Fig. 12 shows the total strain at peak load for two different simulations of the same specimen shown in Fig. 6—type A. In Fig. 12a, blowholes are

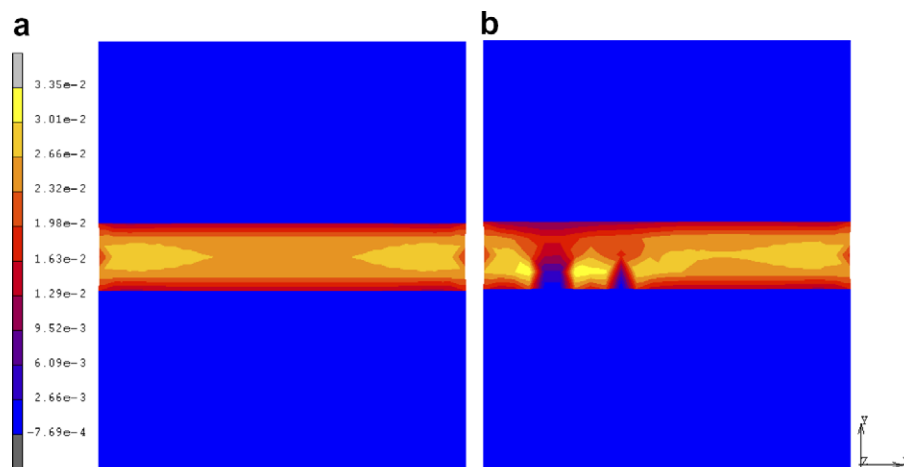

Fig. 12. Simulation of specimen type A shown in Fig. 6, local strain distribution in the loading direction ε_{yy}, with (right) and without (left) the blowholes.

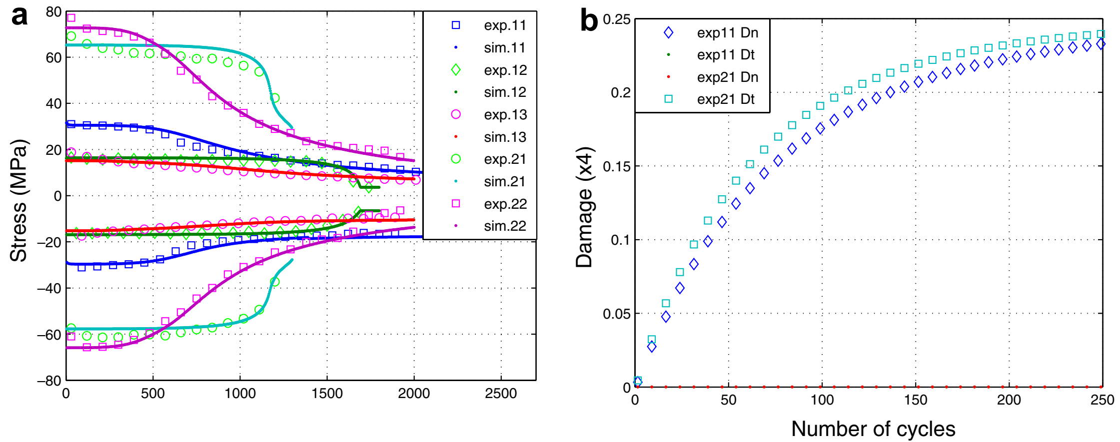

Fig. 13. (a) Comparison of experimental results and numerical calculations, (b) damage evolution in a surface cz element via cyclic loading.

Table 1
Cohesive zone parameters for normal and tangential direction characterizing interfacial separation in a SnAgCu solder joint under cyclic loading

Tensile experiments	Gage width	ε^{peak} (%)	c_n (N/mm)	m_n	r
Exp 11	5 mm	2.0	68,000	3.16	1e-6
Exp 12	1 mm	1.7	68,000	3.16	3e-5
Exp 13	3 mm	1.4	68,000	3.16	1e-6
Shear experiments	Gage width	γ^{peak} (%)	c_t (N/mm)	m_t	r
Exp 21	3 mm	1.8	46,000	3.14	4e-5
Exp 22	3 mm	2.9	48,000	3.13	3e-6

neglected and all interface elements have zero initial damage, whereas in b, two blowholes are placed exactly at the positions that they were observed. It is seen that Fig. 12b gives more realistic results by localizing damage on the weaker boundary. In all simulations, observed blowholes are inserted to the mesh, and by this method the effect of a blowhole on the strength of the interface is incorporated into the model.

Fig. 13 shows a number of experiments and the corresponding numerical simulations covering a variety of specimen geometries and applied strains. The model parameters used to predict the curves in Fig. 13a are tabulated in Table 1. From the fitted parameters, c_n, c_t, m_n and m_t are reproducible. As previously discussed, the solder joint interface is stronger under shear loading than tensile loading, which is also apparent from the numerical results; c_n is 1/3 higher than c_t. Parameter r does not show a clear dependence on the loading direction being normal or tangential, however, it takes distinct values depending on the fracture behavior being gradual (type B) or abrupt (type A). Damage evolution in the cohesive zones are shown in Fig. 13b, by selecting a surface cohesive element node for sim.11 (tensile) and sim.21 (shear).

In summary, the strength of SnAgCu/NiAu interface under mechanical fatigue loading is measured and quantified via cohesive zone elements. The damage parameters are identified as $c_n = 68{,}000$, $c_t = 47{,}000$, $m_n = 3.16$ and $m_t = 3.135$. For parameter r, a range is identified, $r_{grad} = 1\text{e-}6$ as the lower bound for gradual fracture and $r_{del} = 4\text{e-}5$ as the upper bound for delamination. It is thereby suggested to use r_{grad} in standard life-time predictions and r_{del} for safe design.

4. Application to SnAgCu solder interconnect

The cohesive zone parameters given above are used to simulate a solder bump having the dimensions 760 μm diameter, 500 μm height and 100 μm thickness in 2D plane stress. The solder material is SnAgCu,

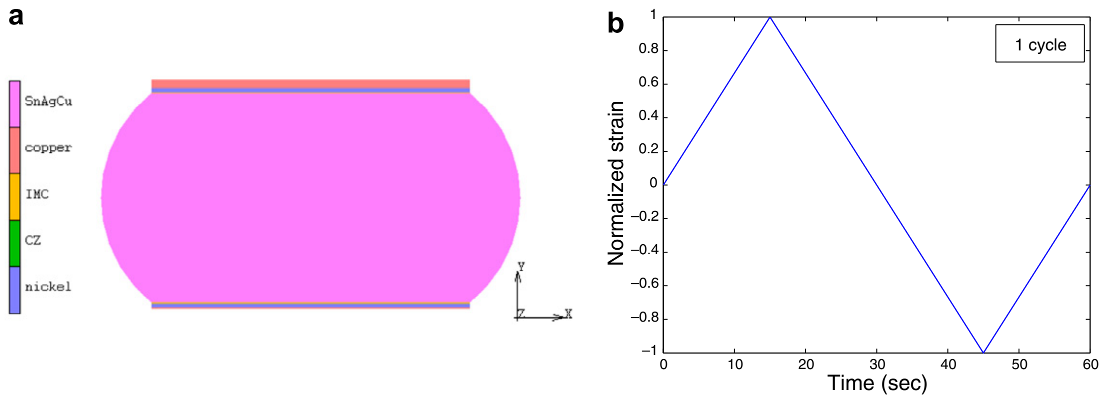

Fig. 14. (a) 2D SnAgCu solder ball with Cu/Ni/Au metallization, (b) prescribed loading on the top middle node ε_{xx}.

metallization is 20 μm copper pad and 10 μm nickel diffusion barrier. Between the metallization and solder, there is a 2 μm thick Ni_3Sn_4 intermetallic layer. Cohesive zone (cz) elements having a 100 nm initial thickness are placed between the solder and the intermetallic layer. Bottom nodes are constrained in both x and y directions, and the middle top node is loaded in cyclic shear. All material properties are the same as in the previous section. Copper is modeled linear elastically with the material parameters $E = 128$ GPa and $\nu = 0.35$. The geometry of the solder bump and the prescribed loading is shown in Fig. 14. Numerical analysis is carried out 1% alternating cyclic strain for 5000 cycles. At each cohesive zone an effective damage value D_{eff} is calculated from the normal and tangential damage components according to the following relation:

$$D_{\text{eff}} = (D_{\text{t}}^2 + D_{\text{n}}^2 - D_{\text{t}}D_{\text{n}})^{\frac{1}{2}} \tag{6}$$

Contour plot of effective damage D_{eff} at the end of cycles $N = 0$, 3000 and 5000 is shown in Fig. 15. For visibility nodal values are linearly averaged in the contour plot. Thus, damage is made visible through the neighboring continuum elements, only for visualization purposes.

The solder ball geometry does not allow to simply justify a plane deformation state. The solder ball model is run with a plane stress and a plane strain assumption. Damage values for the plane stress case is higher than the plane strain case with the same boundary and loading conditions. Thus plane stress assumption provides a lower bound of the fatigue life in the present study, which is preferential from an engineering perspective.

To summarize the discussion so far, an adequate agreement between experimental and numerical work has been established, whereby the cohesive zone approach is proven to be an effective tool in solder joint fatigue failure simulation. The model is numerically stable, and has the potential to be extended to chip size modeling and component life-time predictions. The proposed model has the potential for blowholes to be included in the calculation, provided that adequate data on blowhole size and distribution specific to the manufacturing procedure is known in advance.

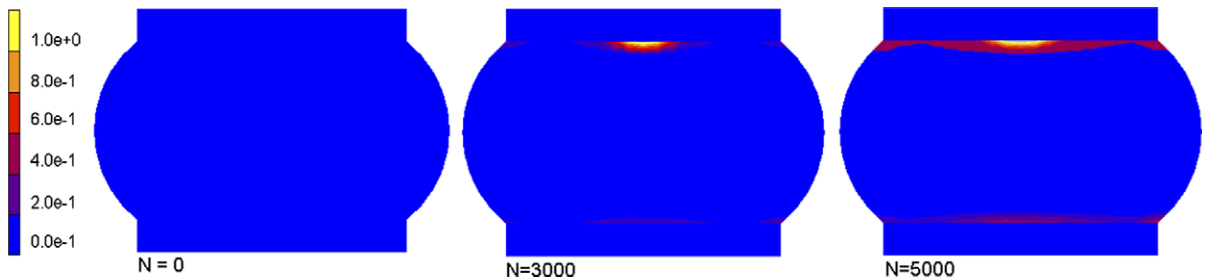

Fig. 15. Effective damage (D_{eff}) in a SnAgCu solder bump after 0, 3000 and 5000 cycles of cyclic shear strain.

5. Conclusions

A combined experimental–numerical study on solder joint fatigue failure is carried out. Ni/Au–SnAgCu solder joints are tested under cyclic shear and cyclic tension for different specimen geometries and strain amplitudes. From the qualitative and quantitative data obtained, interfacial separation due to fatigue damage evolution at the bump/pad interface is simulated using cohesive zone elements. The following conclusions are drawn from the present study:

- From the local strain fields observed in a soldered joint under tensile loading, strain localization is seen to be strongly microstructure dependent. Highest local strains are observed at the solder joint interface followed by grain boundaries.
- Two different microstructural failure mechanisms are observed; i.e., heterogeneous matrix deformation and localization of deformation at the bonding interface. The interfacial failure mode is typically favored at a high initial stress, and small solder volume.
- Strain life of soldered joints is size dependent.
- A strain life fatigue limit for the SnAgCu–Ni/Au bonding interface is observed.
- Cohesive zone material parameters for bump/pad fatigue crack propagation have been established for normal and tangential directions separately using different sample geometries and strain amplitudes.
- An adequate agreement between experimental and numerical work has been established, whereby the cohesive zone approach is proven to be an effective tool in solder joint fatigue failure simulation. The model is numerically stable, and has the potential to be extended to chip size modeling and component life-time predictions.

At present, a mechanical model for cyclic mechanical loading has been established. This study will be complemented by thermally cycled non-constrained solder specimens, in order to quantify the bulk damage in the solder due to thermal cycling. Both mechanical and thermal damage mechanisms will be combined in the future to predict thermo-mechanical damage in solder balls in a BGA assembly.

Acknowledgements

This research is supported by the Technology Foundation STW, applied science division of NWO and the technology programme of the Ministry of Economic Affairs. Special thanks to M.H.M. Kouters for his contribution to the experimental work and to G.Q. Zhang for the valuable discussions.

References

Abdul-Baqi, A., Schreurs, P.J.G., Geers, M.G.D., 2005. Fatigue damage modeling in solder interconnects using a cohesive zone approach. International Journal of Solids and Structures 42, 927–942.

Abtew, M., Seldavuray, G., 2000. Lead-free solders in microelectronics. Materials Science and Engineering R 27, 95–141.

Allen, S.L., Notis, M.R., Chromik, R.R., Vinci, R.P., 2004. Microstructural evolution in lead-free solder alloys: Part 1. Cast Sn–Ag–Cu eutectic. Journal of Materials Research 19, 1417–1431.

Aramis v 5.3.0 User's Manual, 2004. GOM GmbH, Gesellschaft fur Optische Messtechniek.

Barenblatt, G.I., 1962. The mathematical theory of equilibrium cracks in brittle fracture. Advances in Applied Mechanics VII, 55–129.

Chaboche, J.L., Feyel, F., Monerie, Y., 2001. Interface debonding models: a viscous regularization with a limited rate dependency. International Journal of Solids and Structures 38, 3127–3160.

de-Andres, A., Perez, J.L., Ortiz, M., 1999. Elastoplastic finite element analysis of three-dimensional fatigue crack growth in aluminum shafts subjected to axial loading. International Journal of Solids and Structures 36, 2231–2258.

Dugdale, D.S., 1960. Yielding in steel sheets containing slits. Journal of the Mechanics and Physics of Solids 8, 100–104.

Erinc, M., Schreurs, P.J.G., Zhang, G.Q., Geers, M.G.D., 2004. Characterization and fatigue damage simulation in SAC solder joints. Microelectronics Reliability 44, 1287–1292.

Erinc, M., Schreurs, P.J.G., Zhang, G.Q., Geers, M.G.D., 2005. Microstructural damage analysis of SnAgCu solder joints and an assessment on indentation procedures. Journal of Materials Science: Materials in Electronics 16, 93–700.

Foulk, J.W., Allen, D.H., Helms, K.L.E., 1998. A model for predicting the damage and environmental degradation dependent life of SCS-6/Timetal21S$[0]_4$ metal matrix composite. Mechanics of Materials 29, 53–68.

Jang, G.Y., Lee, J.W., Duh, J.G., 2004. The nanoindentation characteristics of Cu_6Sn_5, Cu_3Sn, and Ni_3Sn_4 intermetallic compounds in the solder bump. Journal of Electronics Materials 33, 1103–1110.

Lee, W.W., Nguyen, L.T., Selvaduray, G.S., 2000. Solder joint fatigue models: review and applicability to chip scale packages. Microelectronics Reliability 40, 231–244.

Lin, C.K., Chu, D.Y., 2005. Creep rupture of lead-free Sn–3.5Ag and Sn–3.5Ag–0.5Cu solders. Journal of Materials Science: Materials in Electronics 16, 355–365.

Matin, M.A., 2005. Microstructure evolution and thermo-mechanical fatigue of solder materials. Ph.D Thesis, Technische Universiteit Eindhoven, ISBN 90-386-2887-0.

Metals Handbook, 1985. 9th ed., Mechanical Testing, vol.8. Fatigue Testing, 361–437.

Needleman, A., 1990. An analysis of decohesion along an imperfect interface. International Journal of Fracture 42, 21–40.

Ratchev, P., Vandevelde, B., de Wolf, I., 2004. Reliability and failure analysis of Sn–Ag–Cu solder interconnections for PSGA packages on Ni/Au surface finish. IEEE Transactions on Device and Materials Reliability 4, 5–10.

Roe, K.L., Siegmund, T., 2003. An irreversible cohesive zone model for interface fatigue crack growth simulation. Engineering Fracture Mechanics 70, 209–232.

Sharif, A., Chan, Y.C., 2005. Interfacial reactions of Sn–3.5%Ag and Sn–3.5%Ag–0.5%Cu solder with electroless Ni/Au metallization during multiple reflow cycles. Journal of Materials Science: Materials in Electronics 16, 153–158.

Towashiraporn, P., Subbarayan, G., Desai, C.S., 2005. A hybrid model for computationally efficient fatigue fracture simulations at microelectronic assembly interfaces. International Journal of Solids and Structures 42, 4468–4483.

Van den Bosch, M.J., Schreurs, P.J.G., Geers, M.G.D., 2006. An improved description of the exponential Xu and Needleman cohesive zone law for mixed-mode decohesion. Engineering Fracture Mechanics 73, 1220–1234.

Visser, J.W.W., 2002. Microstructure and deformation analysis of lead-free solder joints. Technische Universiteit Eindhoven, MT02.12.

Wiese, S., Wolter, K.-J., 2004. Microstructure and creep behaviour of eutectic SnAg and SnAgCu solders. Microelectronics Reliability 44, 1923–1931.

Wiese, S., Feustel, F., Meusel, E., 2002. Characterisation of constitutive behaviour of SnAg, SnAgCu and SnPb solder in flip chip solder joints. Sensors and Actuators A 99, 188–193.

Yoon, J., Kim, S., Jung, S., 2005. IMC morphology, interfacial reaction and joint reliability of Pb-free Sn–Ag–Cu solder on electrolytic Ni BGA substrate. Journal of Alloys and Compounds 392, 247–252.

Zeng, K., Vuorinen, V., Kivilahti, J.K., 2002. Interfacial reactions between lead-free SnAgCu solder and Ni(P) surface finish on printed circuit boards. IEEE Transactions on Electronics Packaging Manufacturing 25, 162–167.